



<http://www.diva-portal.org>

This is the published version of a paper published in .

Citation for the original published paper (version of record):

Gordeeva, A., Hsu, Y-J., Jenei, I Z., Carvalho, P H., Simak, S I. et al. (2020)  
Layered Zinc Hydroxide Dihydrate,  $\text{Zn}_5(\text{OH})_{10} \cdot 2\text{H}_2\text{O}$ , from Hydrothermal Conversion of  $\epsilon\text{-Zn}(\text{OH})_2$  at Gigapascal Pressures and its Transformation to Nanocrystalline ZnO  
*ACS OMEGA*, 5(28): 17617-17627  
<https://doi.org/10.1021/acsomega.0c02075>

Access to the published version may require subscription.

N.B. When citing this work, cite the original published paper.

Permanent link to this version:

<http://urn.kb.se/resolve?urn=urn:nbn:se:umu:diva-174504>

# Layered Zinc Hydroxide Dihydrate, $\text{Zn}_5(\text{OH})_{10} \cdot 2\text{H}_2\text{O}$ , from Hydrothermal Conversion of $\epsilon\text{-Zn}(\text{OH})_2$ at Gigapascal Pressures and its Transformation to Nanocrystalline ZnO

Alisa Gordeeva, Ying-Jui Hsu, Istvan Z. Jenei, Paulo H. B. Brant Carvalho, Sergei I. Simak, Ove Andersson, and Ulrich Häussermann\*



Cite This: *ACS Omega* 2020, 5, 17617–17627



Read Online

ACCESS |



Metrics & More

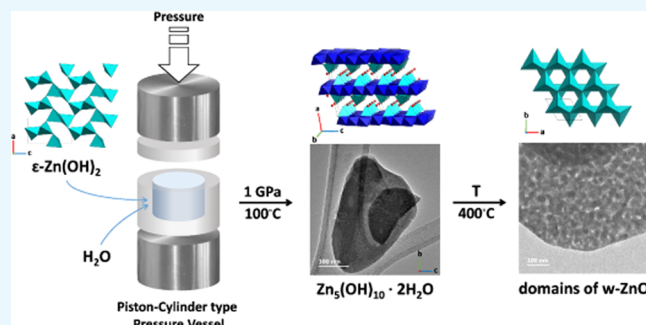


Article Recommendations



Supporting Information

**ABSTRACT:** Layered zinc hydroxides (LZHs) with the general formula  $(\text{Zn}^{2+})_x(\text{OH}^-)_{2x-my}(\text{A}^{m-})_y \cdot n\text{H}_2\text{O}$  ( $\text{A}^{m-} = \text{Cl}^-, \text{NO}_3^-, \text{ac}^-, \text{SO}_4^{2-}$ , etc) are considered as useful precursors for the fabrication of functional ZnO nanostructures. Here, we report the synthesis and structure characterization of the hitherto unknown “binary” representative of the LZH compound family,  $\text{Zn}_5(\text{OH})_{10} \cdot 2\text{H}_2\text{O}$ , with  $\text{A}^{m-} = \text{OH}^-$ ,  $x = 5$ ,  $y = 2$ , and  $n = 2$ .  $\text{Zn}_5(\text{OH})_{10} \cdot 2\text{H}_2\text{O}$  was afforded quantitatively by pressurizing mixtures of  $\epsilon\text{-Zn}(\text{OH})_2$  (wulfingite) and water to 1–2 GPa and applying slightly elevated temperatures, 100–200 °C. The monoclinic crystal structure was characterized from powder X-ray diffraction data (space group  $\text{C2}/c$ ,  $a = 15.342(7)$  Å,  $b = 6.244(6)$  Å,  $c = 10.989(7)$  Å,  $\beta = 100.86(1)^\circ$ ). It features neutral zinc hydroxide layers, composed of octahedrally and tetrahedrally coordinated Zn ions with a 3:2 ratio, in which  $\text{H}_2\text{O}$  is intercalated. The interlayer  $d(200)$  distance is 7.53 Å. The H-bond structure of  $\text{Zn}_5(\text{OH})_{10} \cdot 2\text{H}_2\text{O}$  was analyzed by a combination of infrared/Raman spectroscopy, computational modeling, and neutron powder diffraction. Interlayer  $\text{H}_2\text{O}$  molecules are strongly H-bonded to five surrounding OH groups and appear orientationally disordered. The decomposition of  $\text{Zn}_5(\text{OH})_{10} \cdot 2\text{H}_2\text{O}$ , which occurs thermally between 70 and 100 °C, was followed in an in situ transmission electron microscopy study and ex situ annealing experiments. It yields initially 5–15 nm sized hexagonal w-ZnO crystals, which, depending on the conditions, may intergrow to several hundred nm-large two-dimensional, flakelike crystals within the boundary of original  $\text{Zn}_5(\text{OH})_{10} \cdot 2\text{H}_2\text{O}$  particles.



## 1. INTRODUCTION

Layered zinc hydroxides (LZHs) are considered interesting materials for intercalation and anion exchange, as well as precursors toward (functional) porous ZnO nanostructures.<sup>1–4</sup> LZHs are part of a larger family of layered hydroxide salts with the chemical formula  $\text{M}(\text{II})_x(\text{OH}^-)_{2x-my}(\text{A}^{m-})_y \cdot n\text{H}_2\text{O}$ , where  $\text{M}(\text{II}) = \text{Mg}, \text{Mn–Zn}$  and  $\text{A}^{m-}$  is, e.g.,  $\text{Cl}^-, \text{NO}_3^-, \text{SO}_4^{2-}$ , and  $\text{CO}_3^{2-}$ .<sup>2–5</sup> The layer structure is related to brucite,  $\text{Mg}(\text{OH})_2$ , and features edge-sharing sheets of octahedral zinc hydroxide units where two tetrahedrally coordinated Zn ions are situated above and below vacant octahedral sites. The basal planes of a pair of opposite tetrahedra are then equivalent to opposite triangular units of the empty octahedra. Layers are terminated by an additional ligand, which coordinates the apical site of the tetrahedra.

LZH layers may be (positively) charged or neutral, depending on whether the terminating ligand is water or  $\text{A}^{m-}$ . Figure 1 illustrates the building principle of LZHs with the simple examples  $\text{Zn}_5(\text{OH})_8(\text{NO}_3)_2 \cdot 2\text{H}_2\text{O}$ <sup>6</sup> and  $\text{Zn}_5(\text{OH})_8\text{Cl}_2 \cdot \text{H}_2\text{O}$  (simonkolleite).<sup>7</sup> In both cases, 1/4 of the octahedrally coordinated Zn within a layer is replaced by

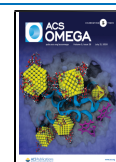
pairs of tetrahedra, i.e., the  $\text{Zn}_o/\text{Zn}_t$  ratio is 3:2; however, their distribution is different, resulting in orthorhombic and trigonal layer symmetries for the nitrate and chloride, respectively. For the former, the terminating ligand is  $\text{H}_2\text{O}$ , and  $\text{NO}_3^-$  ions are intercalated. For the latter, the terminating ligand is  $\text{Cl}^-$ , and neutral  $\text{H}_2\text{O}$  is intercalated. The stacking of layers yields, then, an overall monoclinic and rhombohedral structure for the nitrate and chloride, respectively. Generally, interlayer spacings are comparatively small for LZHs with neutral layers (i.e., for which layers are held together only by a hydrogen-bond network).<sup>5,7</sup>

LZHs can be modified in numerous ways. More complicated structural patterns and different  $\text{Zn}_t/\text{Zn}_o$  ratios may arise when

Received: May 5, 2020

Accepted: June 19, 2020

Published: July 6, 2020



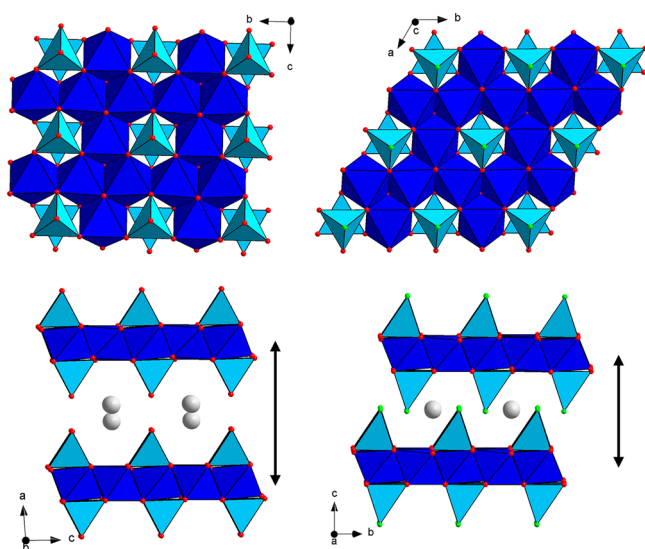


**Figure 1.** Crystal structures of monoclinic  $\text{Zn}_5(\text{OH})_8(\text{NO}_3)_2 \cdot 2\text{H}_2\text{O}$  (left panel) and rhombohedral  $\text{Zn}_5(\text{OH})_8\text{Cl}_2 \cdot \text{H}_2\text{O}$  (right panel). The top row shows the layer of edge-sharing octahedra (dark blue) with different arrangements of vacant sites where two tetrahedrally coordinated Zn ions (light blue) are situated above and below. Their apex atoms define the thickness of a layer. The bottom row shows the stacking of layers. Intercalating species ( $\text{NO}_3^-$  (left) and  $\text{H}_2\text{O}$  (right)) are depicted as gray circles. The basal spacing between layers is indicated by arrows.

anions are divalent,  $\text{A}^{2-}$ . For example,  $\text{SO}_4^{2-}$  replaces  $\text{OH}^-$  from octahedrally coordinated Zn within the sheets.<sup>4,5</sup> Further, terminating layers with hydrophobic long-chain carboxylate ions lead to unique architectures of layer assemblies, which can be subsequently exfoliated.<sup>8–10</sup> Films of LZHs may be prepared by electrodeposition<sup>4</sup> or liquid–liquid biphasic synthesis.<sup>11</sup> Using hydrophilic substrates allows the fabrication of films of upright-standing nanosheets of LZHs that are stacked parallel to the substrate.<sup>12</sup> Depending on the precursor and the treatment procedure, subsequent conversion of LZHs by thermal decomposition results, then, in various nanostructured and nanoporous forms of  $\text{ZnO}$ .<sup>4,12–15</sup>

The simplest representative of the LZH family would be  $\text{A}^{m-} = \text{OH}^-$ , reducing the LZH to binary zinc hydroxide hydrates  $\text{Zn}(\text{OH})_2 \cdot n\text{H}_2\text{O}$  with octahedrally and tetrahedrally coordinated  $\text{Zn}^{2+}$ . In this work, we show that the hydrothermal conversion of  $\epsilon\text{-Zn}(\text{OH})_2$  (wulffite) at high pressures, 1–2 GPa, and moderate temperatures, 100–200 °C, quantitatively produces the zinc hydroxide dihydrate  $\text{Zn}_5(\text{OH})_8(\text{OH})_2 \cdot 2\text{H}_2\text{O}$ .

## 2. RESULTS AND DISCUSSION

**2.1. Synthesis and Crystal Structure Characterization of  $\text{Zn}_5(\text{OH})_{10} \cdot 2\text{H}_2\text{O}$ .** Our hydrothermal conversion experiments of  $\epsilon\text{-Zn}(\text{OH})_2$  targeted pressures up to 2 GPa and employed a large proportion of water (molar ratio 1:55, corresponding to a 1 M situation if referring to a solution) to ensure a constant activity in possible high- $p,T$  processes. The evolution of products is summarized in Figure 2. Autoclave experiments, referring to near-ambient pressure, and piston-cylinder experiments at 0.5 GPa produced hexagonal (wurtzite) w-ZnO. The powder X-ray diffraction (PXRD) pattern of the product obtained at 1 GPa and 100 °C (“1–100” product) revealed a new and unknown phase. In addition,

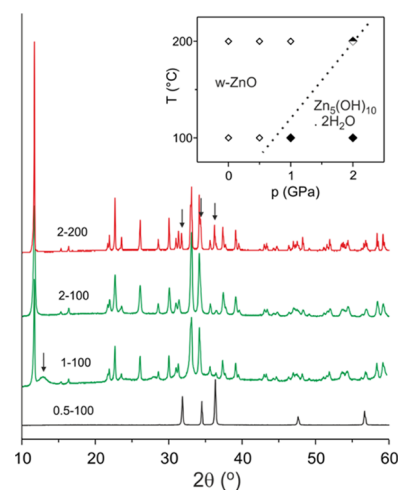


**Figure 2.** PXRD patterns of products obtained from hydrothermal treatment of  $\epsilon\text{-Zn}(\text{OH})_2$  at 100 °C (black and green, bottom) and 200 °C (red, top) at pressures of 0.5, 1, and 2 GPa. Samples are abbreviated as “ $x$ – $y$ ,” where  $x$  is the pressure in GPa and  $y$  is the temperature in °C. The arrow in the 1–100 pattern indicates a reflection of an unknown, largely amorphous phase, whereas the arrows in the 2–200 pattern mark the most prominent peaks from w-ZnO (according to JCPDS Card No. 00-036-1451). The inset shows a pressure–temperature map of the  $\text{Zn}(\text{OH})_2 \cdot \text{H}_2\text{O}$  system.

a pronounced amorphous background was noticeable, along with a very broad reflection centered at  $2\theta \approx 12^\circ$  ( $d \approx 8$  Å). The amorphous feature is absent in the pattern of the 2–100 product, indicating higher crystallinity. Reflections are sharper in the PXRD pattern of the 2–200 product, indicating a larger particle size. At the same time, these conditions produced a small fraction of w-ZnO. The experiment at 1 GPa and 200 °C quantitatively yielded w-ZnO.

The unknown phase was afforded as a fine white powder. The 2–100 product consisted of submicron-sized crystals with a pronounced platelike morphology, whereas the 2–200 product corresponded to seemingly euhedral tabular crystals with sizes up to 10  $\mu\text{m}$  (Figure 3). At higher magnification, however, it is seen that these crystals represent agglomerates of laminar crystals. Electron energy loss and electron-dispersive X-ray spectroscopy analysis showed that the unknown phase is composed of Zn and O, which occurred in a ratio  $\sim 0.4$  (see the Supporting Information, Figures S1 and S2).

The PXRD pattern of the 2–100 product was indexed to a C-centered monoclinic lattice and unit cell parameters were refined as  $a = 15.342(7)$  Å,  $b = 6.244(6)$  Å,  $c = 10.989(7)$  Å, and  $\beta = 100.86(1)^\circ$ . Systematic absences of reflections  $h0l$ ,  $h$ ,  $l \neq 2n$  in the pattern agree with the space group  $\text{C2}/c$  (no. 15). We note that initially a smaller unit cell with a halved  $c$  parameter (5.494 Å) was extracted (with  $\text{C2}/m$  as the suggested space group (no. 12)). However, when solving and subsequently refining the crystal structure, it was deemed appropriate to employ the larger  $c$ -axis. The final Rietveld fit is shown in Figure 4, and Tables 1 and 2 summarize the refinement results and structure parameters.

The unit cell contains 20 Zn atoms, which distribute on two general positions (8f) and on a site 4e (0,  $y$ , 1/4), and 48 O atoms (all on general positions). Zn1 (8f) and Zn2 atoms (4e) attain an octahedral coordination and Zn3 atoms (8f) attain a tetrahedral coordination. Thus,  $\text{ZnO}_6$  octahedra and  $\text{ZnO}_4$  tetrahedra occur in a 12:8 (3:2) ratio and are arranged in layers

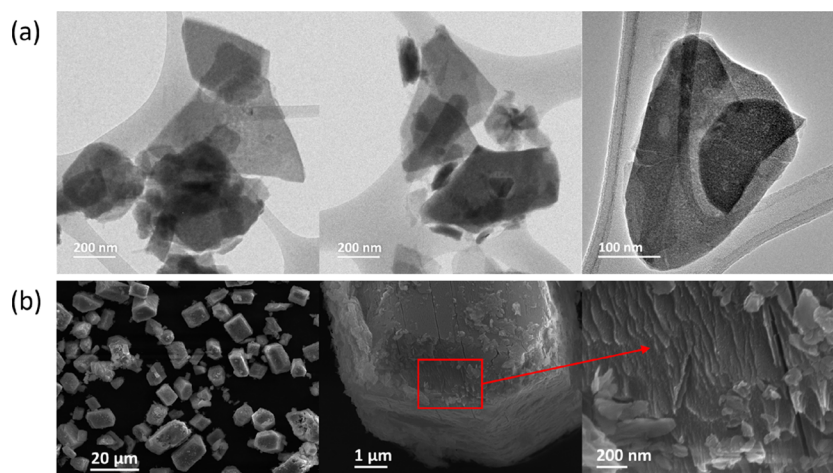


**Figure 3.** (a) Transmission electron microscopy (TEM) images of the product obtained at 2 GPa and 100°C (2–100) taken with different magnifications. (b) Scanning electron microscopy (SEM) images of 2–200 taken with different magnifications. The rugged surface of crystals is attributed to carbonate formation from CO<sub>2</sub> uptake upon exposure to air.

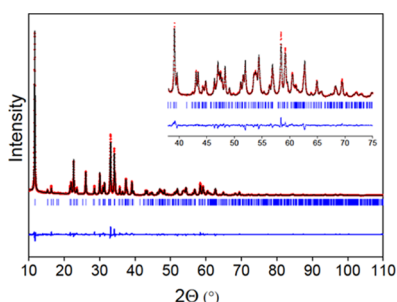


**Figure 4.** Rietveld fit of the Zn<sub>5</sub>(OH)<sub>10</sub>·2H<sub>2</sub>O structure to Cu Kα<sub>1</sub> PXRD data. The inset shows an enlarged section for the 2θ range 38–75°.

**Table 1. Crystal Data and Structure Refinement Results for Zn<sub>5</sub>(OH)<sub>10</sub>·2H<sub>2</sub>O from PXRD Data**

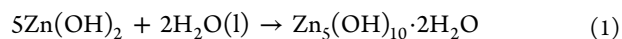
empirical formula	Zn <sub>5</sub> (OH) <sub>10</sub> ·2H <sub>2</sub> O
formula weight, (g/mol)	533.05
temperature (K)	295
crystal system	monoclinic
space group	C2/c (no. 15)
Z	4
a (Å)	15.342(7)
b (Å)	6.244(6)
c (Å)	10.989(7)
β (deg)	100.86(1)
volume (Å <sup>3</sup> )	1033.89(1)
R <sub>p</sub> , R <sub>wp</sub> , R <sub>exp</sub>	8.06, 9.62, 5.37
χ <sup>2</sup>	3.207

typical of LZHS. Zn<sub>6</sub>–O and Zn<sub>4</sub>–O distances are in the range 2.03–2.18 and 1.93–2.06 Å, respectively (Table 3), which corresponds closely to other LZHS (e.g., Zn<sub>5</sub>(OH)<sub>8</sub>(NO<sub>3</sub>)<sub>2</sub>·2H<sub>2</sub>O for which *d*(Zn<sub>6</sub>–O) = 2.02–2.19 Å and *d*(Zn<sub>4</sub>–O) 1.94–1.96 Å).<sup>6</sup> Since strongly basic OH<sup>−</sup> ions cannot exist uncoordinated in the presence of H<sub>2</sub>O, we assign OH<sup>−</sup> (carried by O1) as the layer-terminating ligand for Zn<sub>4</sub>. Thus, the layer is neutral and the interlayer O (O6) is part of a water molecule. We, therefore, conclude that the hydrothermal conversion of ε-Zn(OH)<sub>2</sub> at 1–2 GPa and 100–200 °C

affords unprecedented zinc hydroxide dihydrate with a formula Zn<sub>5</sub>(OH)<sub>10</sub>·2H<sub>2</sub>O and Z = 4 in a C/2c unit cell.

The structure of Zn<sub>5</sub>(OH)<sub>10</sub>·2H<sub>2</sub>O is depicted in Figure 5. The distribution of tetrahedral units within layers is identical to that of monoclinic Zn<sub>5</sub>(OH)<sub>8</sub>(NO<sub>3</sub>)<sub>2</sub>·2H<sub>2</sub>O (cf. Figure 1a).<sup>6</sup> However, as initially mentioned, we doubled the translational period in the *c*-direction. The O6 position of the water molecule was refined as (0.250, 0.066, 0.410). For *y* = 0, this position can be expressed as 4*i* (*x*0*z*) in space group C2/*m* with a halved *c* unit cell parameter (*c* ≈ 5.5 Å). This is indicated in Figure 5a. However, the deviation from *y* = 0 appeared significant, and, therefore, the larger *c*-axis was employed. The stacking of layers in the Zn<sub>5</sub>(OH)<sub>10</sub>·2H<sub>2</sub>O structure (along the *a*\*-direction) is similar to Zn<sub>5</sub>(OH)<sub>8</sub>Cl<sub>2</sub>·H<sub>2</sub>O, which also consists of neutral layers.<sup>7</sup> The stacking is very compact in Zn<sub>5</sub>(OH)<sub>10</sub>·2H<sub>2</sub>O. The so-called basal distance (the distance between the centers of two adjacent layers) is *d* ≈ 7.53 Å.

The hydrothermal conversion of ε-Zn(OH)<sub>2</sub> to w-ZnO at close to ambient pressure has been discussed to occur by either dissolution–precipitation or solid-state transformation.<sup>16–19</sup> We conjecture that the hydrothermal transformation of ε-Zn(OH)<sub>2</sub> to Zn<sub>5</sub>(OH)<sub>10</sub>·2H<sub>2</sub>O at high pressure is initiated at the surface of the hydroxide, which produces flakelike hydrate particles with sizes between 10 and 50 nm. Such flakelike particles would peel off the hydroxide surface and subsequently grow, via dissolution–precipitation, to platelike 0.1–0.5 μm sized crystals (i.e., the 1–100 and 2–100 products) that aggregate into particles with a tabular morphology at higher temperatures (i.e., the 2–200 product). The enthalpy of the reaction



can be estimated as +39 kJ/mol under standard conditions (cf. differential scanning calorimetry (DSC) measurements, Section 2.3, and the Supporting Information, Figure S3). Consequently, the transformation is accompanied by a large energy penalty, and Zn<sub>5</sub>(OH)<sub>10</sub>·2H<sub>2</sub>O is metastable at atmospheric pressure and room temperature. High pressure is clearly essential for the synthesis of Zn<sub>5</sub>(OH)<sub>10</sub>·2H<sub>2</sub>O because the volume change for reaction (1) is strongly negative (about −47.3 cm<sup>3</sup>/mol under ambient conditions and



**Table 2. Fractional Atomic Coordinates and Isotropic Equivalent Displacement Parameters for  $\text{Zn}_5(\text{OH})_{10} \cdot 2\text{H}_2\text{O}^a$  from PXRD Data**

atom	Wyck	<i>x</i>	<i>y</i>	<i>z</i>	<i>U</i> <sub>iso</sub> (Å <sup>2</sup> )
Zn1	8 <i>f</i>	0.4983(4)	0.24757(17)	0.0004(5)	0.0577(4)
Zn2	4 <i>e</i>	0	0.0003(10)	0.25	0.0577(4)
Zn3	8 <i>f</i>	0.38168(8)	0.0004(7)	0.21436(12)	0.0577(4)
O1	8 <i>f</i>	0.2533(4)	0.019(2)	0.1632(5)	0.0597(8)
O2	8 <i>f</i>	0.0860(7)	0.2406(18)	0.1912(11)	0.0597(8)
O3	8 <i>f</i>	0.4315(4)	0.486(3)	0.0730(5)	0.0597(8)
O4	8 <i>f</i>	0.4268(8)	0.2597(18)	0.3236(11)	0.0597(8)
O5	8 <i>f</i>	0.0785(4)	0.492(3)	0.4417(5)	0.0597(8)
O6	8 <i>f</i>	0.2497(4)	0.0660(13)	0.4098(7)	0.0710(3)

<sup>a</sup>C2/c, Z = 4, T = 295 K, estimated standard deviations in parentheses.

**Table 3. Interatomic Distances (<3.0 Å) for  $\text{Zn}_5(\text{OH})_{10} \cdot 2\text{H}_2\text{O}$  from PXRD Data<sup>a</sup>**

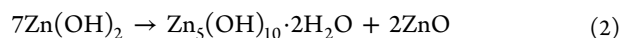
atom 1	atom 2	distance (Å)	atom 1	atom 2	distance (Å)
Zn1	O3	2.052(15)	O1	O6	2.737(10)
	O4	2.056(12)		O6	2.825(10)
	O5	2.113(15)		O6	2.938(15)
	O5	2.150(15)		O2	2.982(14)
	O3	2.214(15)		O3	2.945(15)
	O2	2.255(12)		O1	2.982(14)
Zn2	O3	2.031(5)	O3	O4	2.661(16)
	O3	2.031(5)		O6	2.866(10)
	O4	2.124(13)		O3	2.880(9)
	O4	2.124(13)		O2	2.945(15)
	O2	2.175(12)		O3	2.661(16)
	O2	2.175(12)		O5	2.959(16)
Zn3	O5	1.926(6)	O5	O6	2.850(8)
	O2	1.939(12)		O5	2.935(9)
	O1	1.947(6)		O4	2.959(16)
	O4	2.056(12)		O1	2.737(10)
				O1	2.825(10)
				O5	2.850(8)
				O3	2.661(16)
				O1	2.938(15)

<sup>a</sup>Estimated standard deviations are given in parentheses.

estimated to be around  $-40 \text{ cm}^3/\text{mol}$  under the conditions of synthesis). Thus, the  $pV$  term (integral of  $\Delta V dp$  from 1 atm to high pressure) at room temperature and 1 GPa is estimated to be about  $-47.3 \text{ kJ/mol}$  and, therefore, can overcome the destabilizing enthalpy at atmospheric pressure. The contribu-

tion of entropy,  $T\Delta S$ , cannot be readily constrained but will make reaction (1) generally less favorable with increasing temperature.

Note that  $\text{Zn}_5(\text{OH})_{10} \cdot 2\text{H}_2\text{O}$  can also be obtained by heating pressurized  $\epsilon\text{-Zn}(\text{OH})_2$  without a water environment, according to



A PXRD pattern of the product of such an experiment is shown as the Supporting Information, Figure S4. The initial step of this dry transformation should be analogous to the solid-state transformation (in situ crystallization) of  $\epsilon\text{-Zn}(\text{OH})_2$  into  $w\text{-ZnO}$ . Here, the dehydration occurs initially at the surface of hydroxide crystals, leading to cracks and holes due to the much higher density of  $w\text{-ZnO}$ .<sup>16,17</sup> Hydrate formation will then occur at the interface of liberated water with  $\epsilon\text{-Zn}(\text{OH})_2$  and a hydroxide crystal is gradually transformed into a mixture of  $\text{Zn}_5(\text{OH})_{10} \cdot 2\text{H}_2\text{O}$  and  $w\text{-ZnO}$ .

Finally,  $\text{Zn}_5(\text{OH})_{10} \cdot 2\text{H}_2\text{O}$  can be prepared as a completely deuterated sample when performing the hydrothermal conversion of  $\epsilon\text{-Zn}(\text{OH})_2$  in a heavy water ( $\text{D}_2\text{O}$ ) environment. Metastable  $\text{Zn}_5(\text{OH})_{10} \cdot 2\text{H}_2\text{O}$  appears to decompose over time (several months) even when stored under inert, moisture-free, conditions. Exposure to air leads to a rapid loss of crystallinity of samples due to carbonate formation from the incorporation of  $\text{CO}_2$ ; cf. Figure S5a,b in the Supporting Information.

**2.2. Investigations into the Hydrogen-Bond Structure of  $\text{Zn}_5(\text{OH})_{10} \cdot 2\text{H}_2\text{O}$ .** General information on the coordination environment of hydroxide ions and hydrogen bonding can be obtained from IR and Raman spectroscopic measure-

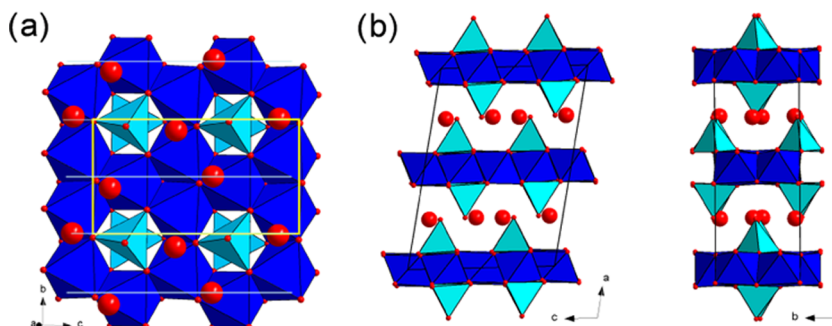


**Figure 5.** Structure of  $\text{Zn}_5(\text{OH})_{10} \cdot 2\text{H}_2\text{O}$ . (a) Layer of edge-sharing octahedra (dark blue) and tetrahedra (light blue) sitting above and below vacant octahedral sites. Interlayer water molecules are represented as large red spheres. Their breaking of the  $2/m$  mirror symmetry causes a doubling of the  $c$  parameter as compared to  $\text{Zn}_5(\text{OH})_8(\text{NO}_3)_2 \cdot 2\text{H}_2\text{O}$  (cf. Figure 1). (b) Stacking of layers viewed along the  $b$ - (left) and  $c$ -directions (right).

ments.<sup>20–22</sup> Here, it is instructive to compare  $\epsilon$ -Zn(OH)<sub>2</sub> and Zn<sub>5</sub>(OH)<sub>10</sub>·2H<sub>2</sub>O, and Figure 6 shows the attenuated total

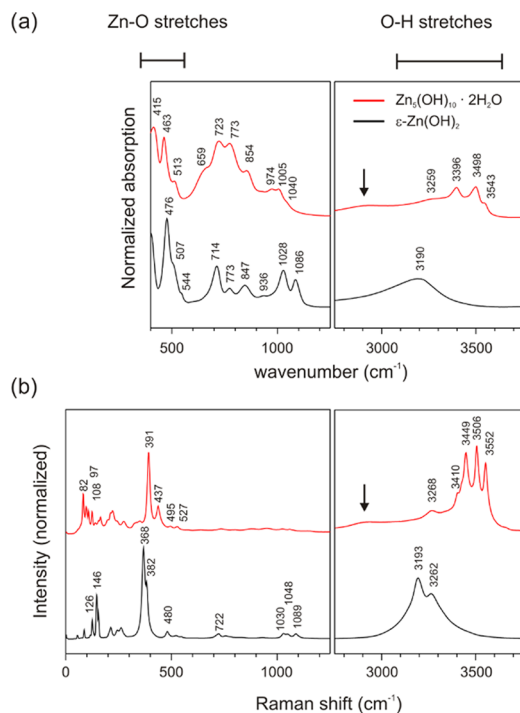


**Figure 6.** ATR-FTIR (a) and Raman spectra (b) of  $\epsilon$ -Zn(OH)<sub>2</sub> and Zn<sub>5</sub>(OH)<sub>10</sub>·2H<sub>2</sub>O (black and red lines, respectively). The arrows mark a feature at  $\sim 2900$  cm<sup>−1</sup> that most likely corresponds to a broad O–H stretching band.

reflection Fourier transform infrared (ATR-FTIR) and Raman spectra of both compounds. The vibrational properties of  $\epsilon$ -Zn(OH)<sub>2</sub> have been reported and analyzed earlier.<sup>23,24</sup> In  $\epsilon$ -Zn(OH)<sub>2</sub>, Zn ions are tetrahedrally coordinated by four OH<sup>−</sup> ions, at distances between 1.94 and 1.96 Å, and each OH<sup>−</sup> ion is shared by two Zn ions. The topology of the arrangement of Zn(OH)<sub>4</sub> tetrahedra is equivalent to that of SiO<sub>4</sub> tetrahedra in  $\beta$ -cristobalite.<sup>25</sup> The vibrational spectrum of  $\epsilon$ -Zn(OH)<sub>2</sub> can be divided into four regions. At the highest wavenumbers (above 3000 cm<sup>−1</sup>) are the O–H stretching modes from the two crystallographically independent OH groups. Those appear as a broad band centered at around 3200 cm<sup>−1</sup> in the IR spectrum but split in the Raman spectrum (3193 and 3262 cm<sup>−1</sup>). The comparatively low (red-shifted) wavenumbers of these bands with respect to the free OH<sup>−</sup> ion ( $\sim 3550$  cm<sup>−1</sup>) signal the strong O–H $\cdots$ O hydrogen bonding in  $\epsilon$ -Zn(OH)<sub>2</sub>.<sup>24</sup> The spectral range of Zn–OH bends (which are also called OH librations)<sup>20</sup> is between 600 and 1200 cm<sup>−1</sup>. Zn–O stretches fall in the region between 350 and 600 cm<sup>−1</sup>. The asymmetric stretches (with a high IR intensity) are in the range 470–550 cm<sup>−1</sup>, whereas the symmetric ones are seen at 368 and 382 cm<sup>−1</sup> in the Raman spectrum.<sup>24</sup> Bands below 350 cm<sup>−1</sup>, as seen in the Raman spectrum, belong to lower energy lattice modes.

Zn<sub>5</sub>(OH)<sub>10</sub>·2H<sub>2</sub>O possesses four crystallographically independent OH groups (when referring to the smaller C2/m unit cell) and one water molecule. Thus, one expects six O–H stretching modes. In the IR and Raman spectra, one can discern clearly four and five bands, respectively, which are associated with O–H stretches. Compared to  $\epsilon$ -Zn(OH)<sub>2</sub>, the

majority is at noticeably higher wavenumbers (in a range from 3400 to 3550 cm<sup>−1</sup>), which manifests considerably weaker H bonding. One band at  $\sim 3260$  cm<sup>−1</sup>, however, is in the range of the O–H bands of  $\epsilon$ -Zn(OH)<sub>2</sub> and there is a broad band at 2900 cm<sup>−1</sup>, which is consistently seen in both Raman and IR spectra, indicating very strong H bonding. It is usually very difficult to discriminate O–H stretches of water from hydroxyl since they appear in the same spectral region. Sometimes, they can be distinguished by their normally larger half-widths.<sup>20</sup> Thus, the broad bands at  $\sim 3260$  and 2900 cm<sup>−1</sup> possibly associate with the water molecule. In the spectrum of deuterated Zn<sub>5</sub>(OD)<sub>10</sub>·2D<sub>2</sub>O, O–D stretching modes are shifted to the range 2200–2650 cm<sup>−1</sup>, and O–H and O–D modes relate consistently through an isotope shift  $\sim 1.34$ . Importantly, this includes the broad peak at 2900 cm<sup>−1</sup>, which is shifted to  $\sim 2200$  cm<sup>−1</sup> (see Figure S6 in the Supporting Information).

The water bending mode is expected at around 1600 cm<sup>−1</sup>,<sup>22,23</sup> but it was not possible to see this feature in either the IR or Raman spectrum of Zn<sub>5</sub>(OH)<sub>10</sub>·2H<sub>2</sub>O. The OH librational (Zn–OH bending) region is very similar to  $\epsilon$ -Zn(OH)<sub>2</sub>, but bands are less resolved for Zn<sub>5</sub>(OH)<sub>10</sub>·2H<sub>2</sub>O due to the more complex nature and larger number of modes. Also, it is not possible to discriminate Zn<sub>1</sub>–O from Zn<sub>6</sub>–O stretches clearly. The latter are expected to appear at somewhat lower wavenumbers. It is possible, but not obvious, that the band at 415 cm<sup>−1</sup> in the IR spectrum and the band at 391 cm<sup>−1</sup> in the Raman spectrum relate to Zn<sub>6</sub>–O stretching modes.

To investigate the arrangement of H atoms, we conducted a constraint structure prediction using a simple repulsion potential for the charged ions. The positions of the Zn and O atoms corresponded to the experimental PXRD structure and were not varied. Several simulated annealing global optimization runs with 50–100 seeds and various speeds were completed. As a result, a range of structures with different hydrogen positions was collected and subsequently subjected to density functional theory (DFT) optimization, now relaxing all atom positions but keeping the unit cell shape fixed to that of the experimental structure. One solution possessed a distinguished low total energy. The parameters of this DFT relaxed structure are given in Table S1 (Supporting Information), and a structure fragment highlighting the H-bond structure is shown in Figure 7a. Table 4 lists the essential interatomic distances of the H-bond structure.

The water molecule appears to be coordinated by five oxygen atoms. There are two donor contacts to tetrahedron-

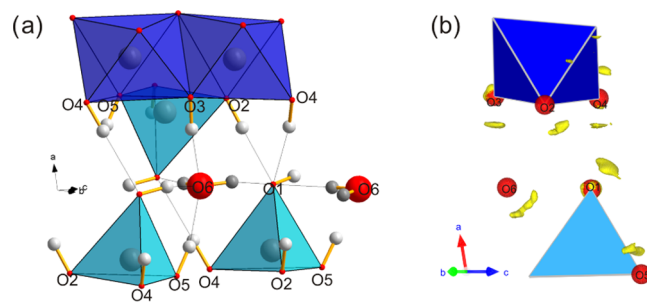


**Figure 7.** (a) DFT relaxed arrangement of H atoms in the Zn<sub>5</sub>(OH)<sub>10</sub>·2H<sub>2</sub>O structure. The hydrogen atoms are represented as light and dark gray spheres when part of OH<sup>−</sup> and H<sub>2</sub>O, respectively. (b) Neutron powder diffraction difference Fourier map of Zn<sub>5</sub>(OD)<sub>10</sub>·2D<sub>2</sub>O.

**Table 4.** H-Bond Structure of  $\text{Zn}_5(\text{OH})_{10} \cdot 2\text{H}_2\text{O}$  from DFT Optimization<sup>a</sup>

O1	<i>d</i> (Å)	O6	<i>d</i> (Å)
O1–H1	0.99	O6–H6	0.99
O1–O6 (H6) A	2.69 (1.79)	O6–H7	1.0
O1–O6 (H1–O6) D	2.85 (1.98)	O6–O1 (H6–O1) D	2.69 (1.79)
O1–O2 (H2) A	2.92 (1.93)	O6–O3 (H3) A	2.82 (1.85)
O1–O6 (H7) A	3.04 (2.05)	O6–O5 (H5) A	2.84 (1.87)
O1–O4 (H4) A	3.19 (2.21)	O6–O1 (H1) A	2.85 (1.98)
		O6–O1 (H7–O1) D	3.04 (2.05)

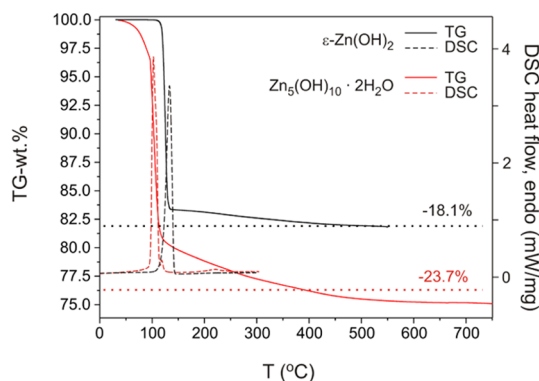
<sup>a</sup>The contacts are distinguished as donor (D) and acceptor (A) contacts.

apex O1 atoms, and three acceptor contacts (to O1–H1, O3–H3, and O5–H5). (Note, for comparison, in the H-bonded structure of hexagonal ice  $I_h$ , each water molecule realizes two donor and two acceptor contacts to four neighboring O atoms). The apex hydroxyl O1–H1 plays a central role in the H-bond structure of  $\text{Zn}_5(\text{OH})_{10} \cdot 2\text{H}_2\text{O}$ . The Zn–OH group is bent drastically with respect to the layer stacking direction and aligns almost with the *bc* plane, where the O6 atom of the water molecules resides. Each O1 acts as an acceptor to two water molecules and O1–H1 acts as a donor to a third water molecule. The H-bond environment of O1 is completed by two additional acceptor contacts to O2–H2 and O4–H4 from the adjacent layer.

Ultimately, the H-bond structure  $\text{Zn}_5(\text{OH})_{10} \cdot 2\text{H}_2\text{O}$  would be revealed from a neutron diffraction study of the deuterated sample. Unfortunately, the small amount and probably limited quality of our (aged) sample prohibited a rigorous determination and refinement of H-atom positions from the collected neutron diffraction data. Figure 7b shows the difference Fourier map calculated from the PXRD refined Zn- and O-atom arrangements. There is residual nuclear density in the vicinity of all O atoms. For the O atoms being part of the layer (O1–O5), they are largely in agreement with the DFT optimized model. However, the residual density around O6 deviates significantly from the localized water molecule in the DFT model. This indicates that water molecules in  $\text{Zn}_5(\text{OH})_{10} \cdot 2\text{H}_2\text{O}$  are orientationally disordered. The nature of this disorder may be dynamical.

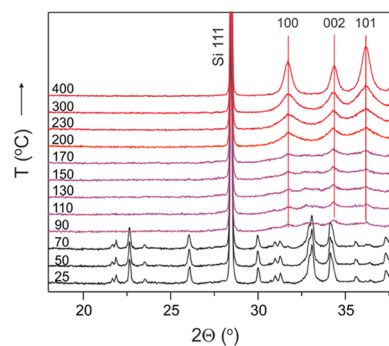
**2.3. Thermal Behavior/Decomposition of  $\text{Zn}_5(\text{OH})_{10} \cdot 2\text{H}_2\text{O}$ .** As initially mentioned, the thermal decomposition of LZHS represents a simple route to ZnO nanostructures, which has been intensively investigated.<sup>4,12–15</sup> In this respect, it is also interesting to probe the thermal behavior of  $\text{Zn}_5(\text{OH})_{10} \cdot 2\text{H}_2\text{O}$ .

Figure 8 shows the thermogravimetric (TG) analysis trace of  $\text{Zn}_5(\text{OH})_{10} \cdot 2\text{H}_2\text{O}$  in comparison with that of  $\epsilon\text{-Zn}(\text{OH})_2$ . The latter shows a clean decomposition at 130 °C with an initial weight loss of about 17%, which increases to the crystallographic water content (18.1%) above 400 °C. This is in good agreement with previous studies.<sup>26,27</sup> The continuous nature of the weight loss above 130 °C indicates gradual release of water, which is attributed to the condensation of surface hydroxyl terminating the initially formed, nanosized, ZnO particles.  $\text{Zn}_5(\text{OH})_{10} \cdot 2\text{H}_2\text{O}$ , which is metastable at standard ambient temperature and pressure, shows immediate weight loss upon heating from room temperature. A steep loss of about 16% is observed at around 100 °C. Above 110 °C, further weight loss of a continuous nature is seen up to about 600 °C. The total weight loss exceeds somewhat the crystallographic water

**Figure 8.** TG curves (solid lines) and DSC traces (broken lines) of  $\epsilon\text{-Zn}(\text{OH})_2$  (black) and  $\text{Zn}_5(\text{OH})_{10} \cdot 2\text{H}_2\text{O}$  (red). The dotted lines indicate calculated weight losses according to the formula units.

content (23.7%). This may be attributed to a comparatively large concentration of surface water and/or the partial conversion of hydrate surfaces into carbonate (cf. Figure 3b and S5b). We note that aged samples (containing carbonate) show an altered TG behavior; see Figure S5c (Supporting Information). Both decomposition reactions, yielding water vapor at the respective decomposition temperatures, are associated with an endothermic signal in DSC experiments (as included in Figure 8). The estimated decomposition enthalpies are 576.2 and 508.2 J/g for  $\text{Zn}_5(\text{OH})_{10} \cdot 2\text{H}_2\text{O}$  and  $\epsilon\text{-Zn}(\text{OH})_2$ , respectively. The decomposition of  $\text{Zn}_5(\text{OH})_{10} \cdot 2\text{H}_2\text{O}$  becomes exothermic with respect to liquid water,  $\sim -4.7$  kJ/mol, whereas the one of  $\epsilon\text{-Zn}(\text{OH})_2$  remains endothermic,  $\sim 6.8$  kJ/mol (cf. Discussion in the Supporting Information, Figure S3).

The thermal decomposition of  $\text{Zn}_5(\text{OH})_{10} \cdot 2\text{H}_2\text{O}$  was then monitored by a multitemperature PXRD investigation, which is shown in Figure 9. The time between two temperature steps is

**Figure 9.** Multitemperature PXRD patterns showing the transformation of  $\text{Zn}_5(\text{OH})_{10} \cdot 2\text{H}_2\text{O}$  (black patterns) to w-ZnO (red patterns). Temperatures are specified in °C.

roughly 1 h (which corresponds to a considerably lower heating rate than that in the TG experiment (5 °C/min)). Diffraction peaks of  $\text{Zn}_5(\text{OH})_{10} \cdot 2\text{H}_2\text{O}$  disappeared above 70 °C. At 110 °C, weak and broad reflections appear, seemingly related to w-ZnO, which, however, are not clearly developed until about 170 °C. Above 300 °C, intensities correspond to that of bulk crystalline w-ZnO (according to JCPDS Card No. 00-036-1451). The broad reflections of the patterns obtained between 150 and 300 °C suggest that the sizes of ZnO particles range from 4 to 20 nm, and the intensity distribution



indicates initial two-dimensional growth in the *ab* plane with preferred orientation along the *c*-direction.

To look into the possibility of an intermediate phase during the thermal conversion of  $\text{Zn}_5(\text{OH})_{10}\cdot 2\text{H}_2\text{O}$ , possible layered  $\text{Zn}(\text{OH})_2$ , an in situ decomposition study in a transmission electron microscope (TEM) was performed (Figure 10). This

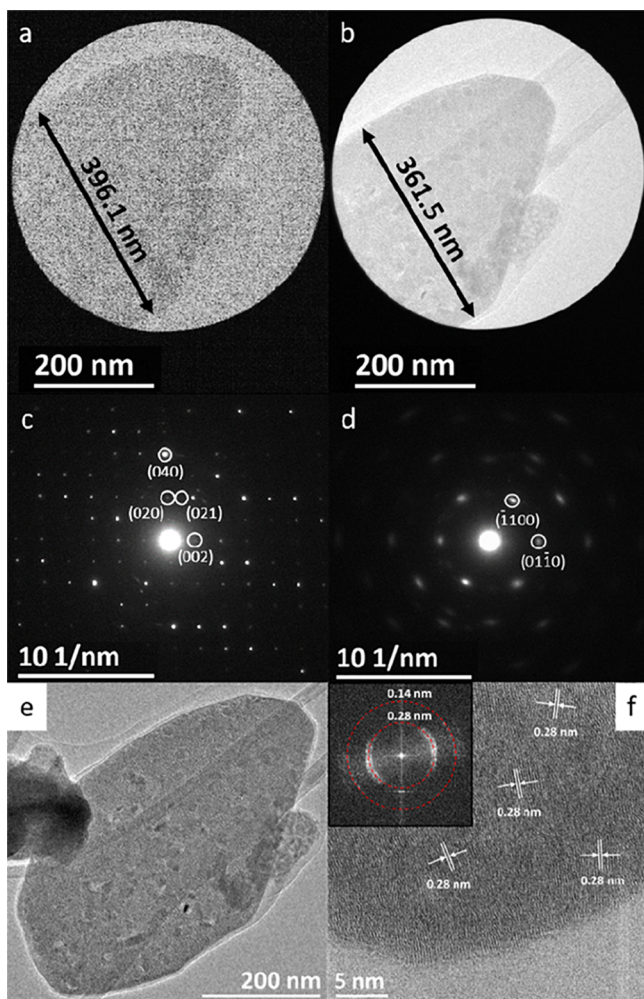


**Figure 10.** TEM bright-field (BF) images of a single crystal of  $\text{Zn}_5(\text{OH})_{10}\cdot 2\text{H}_2\text{O}$  before exposure to the electron beam (a) and after electron beam irradiation for about 40 min (b). The corresponding SAED patterns are shown in (c) and (d). (e) BF image of the whole crystal after 40 min of exposure showing grainy contrasts of inhomogeneity. (f) High-resolution TEM (HRTEM) image with a fast Fourier transform (FFT) inset of a  $\text{Zn}_5(\text{OH})_{10}\cdot 2\text{H}_2\text{O}$  single crystal after 5 min of beam exposure under cryo conditions. Unaligned w-ZnO domains can be seen as regions with differently oriented lattice fringes on the HRTEM image.

exploits the beam damage effect from the inelastic scattering of electrons, and in situ TEM studies have been previously employed to investigate the hydroxide to oxide conversions, e.g., for  $\text{Al}(\text{OH})_3$ ,  $\text{AlO}(\text{OH})$ , and  $\text{In}(\text{OH})_3$ .<sup>28–30</sup> Our study utilized single crystals from the 2–100 product and in the following, we describe an experiment using a crystal about  $300 \times 600 \text{ nm}^2$  in size. Immediately after crystal selection, a bright-field (BF) image and selected area electron diffraction (SAED) pattern were recorded (Figure 10a,c, respectively). The SAED pattern of the  $\text{Zn}_5(\text{OH})_{10}\cdot 2\text{H}_2\text{O}$  crystal before the exposure can be indexed as slightly misaligned along the (100) zone axis,

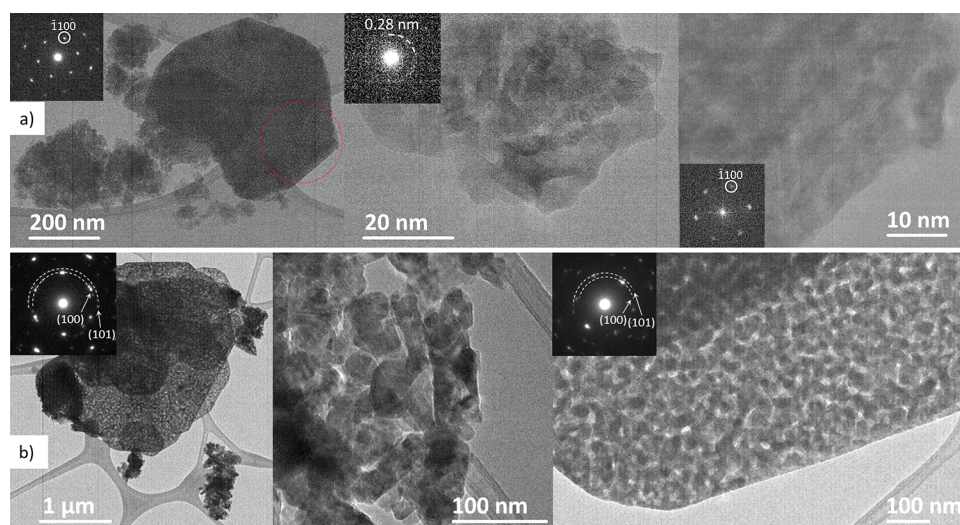
with lattice parameters  $b \approx 6.3 \text{ \AA}$  and  $c \approx 11.0 \text{ \AA}$ . Afterward, consecutive SAED patterns were taken approximately every 45 s until full conversion to w-ZnO, which was achieved after 30–40 min of exposure. The recorded sequence of SAED patterns was compiled into a speeded-up frame-by-frame video of the transformation, which can be found in the Supporting Information. After conversion, the shape of the parent platelike crystal is preserved; however, the linear dimension (width) is reduced by 7–9% (Figure 10b). The SAED pattern of the particle after conversion (Figure 10d) can be identified as the (0001) zone axis of w-ZnO with  $\langle 01\text{--}10 \rangle$  lattice spacings of  $2.8 \text{ \AA}$ . The BF image of the whole particle is shown in Figure 10e. The grainy contrast indicates that the particle is not a homogeneous ZnO crystal but contains interspersed 20–30 nm sized domains.

Figure 10f shows an HRTEM image of a different crystal that was examined under cryo conditions after about 5 min of beam exposure. Here, the decomposition resulted in an aggregation of differently oriented 3–8 nm large nanocrystals. The *d*-spacing between lattice fringes in all nanocrystals is  $2.8 \text{ \AA}$ , corresponding to the (100) lattice planes of w-ZnO. The Fourier transform of the HRTEM image shows a ringlike pattern, which indicates that the maximum local misalignment of the domains is  $\sim 79^\circ$ . This experiment was intended to simulate the mildest applicable decomposition conditions; yet, no intermediate phase was observed. We therefore conclude that the thermal conversion of  $\text{Zn}_5(\text{OH})_{10}\cdot 2\text{H}_2\text{O}$  proceeds directly to w-ZnO.

Compared to other LZHS,  $\text{Zn}_5(\text{OH})_{10}\cdot 2\text{H}_2\text{O}$  is distinguished by its extraordinarily low decomposition temperature due to its metastable nature under ambient conditions. Further, because  $\text{A}^{m-} = \text{OH}^-$ , this decomposition occurs as a single step without the formation and release of a secondary Zn product, which may provide an opportunity to obtain unique forms of w-ZnO. In this work, we did not perform detailed investigations in this direction. However, we followed up the in situ TEM study by ex situ decomposition experiments where parts of the 2–100 sample were placed in preheated environments at 125, 170, and  $400^\circ\text{C}$  for 1 h. The products from the 125 and  $175^\circ\text{C}$  decomposition experiments were very similar and constituted flakelike crystals with sizes of several hundred nm, which resembled the proportions of the original 2–100  $\text{Zn}_5(\text{OH})_{10}\cdot 2\text{H}_2\text{O}$  crystals, and small, 5–15 nm sized, nanocrystals (Figures 11a and S7). This observation confirms the result of the in situ TEM study and may be interpreted as follows: as hydrate crystals break down, w-ZnO nuclei evolve. The subsequent growth and intergrowth of w-ZnO nanocrystals may lead to flakelike crystals within the boundary of the initial hydrate particle. Moreover, this aggregation or intergrowth of nanocrystals toward the formation of homogeneous two-dimensional crystals may be interpreted as “crystallization by particle attachment” (CPA).<sup>31</sup> Nucleation of w-ZnO and crystal growth at first constrained within the initial precursor crystal shape have been observed for other LZHS under certain conditions, and also to occur in an oriented, topotactic-like, fashion.<sup>32,33</sup> From our preliminary studies, it is not possible to draw any comparative conclusions for  $\text{Zn}_5(\text{OH})_{10}\cdot 2\text{H}_2\text{O}$ .

Without sufficient mass transport, the intergrowth is disrupted and nanocrystals are merely agglomerated. It can be assumed that liberated water plays a pivotal role in the mass transport during growth and intergrowth since diffusion of ions should be negligible at such low temperatures. Figure 11b





**Figure 11.** TEM images of ex situ decomposition products of  $\text{Zn}_5(\text{OH})_{10}\cdot 2\text{H}_2\text{O}$  annealed at (a) 170 °C and (b) 400 °C for 1 h. Products of decomposition constitute big flake-like particles and small nanocrystals (left panel). The medium panel highlights the nanocrystal fraction of the sample. Higher magnification images of the big particles (right panel) show a monocrystalline and polycrystalline nature for the 170 and 400 °C decomposition products, respectively. (b, right) is an HRTEM image with FFT in the inset; all other images are BF images with SAED in the insets. The red circle in (a) shows the placement of the SAED aperture.

shows TEM figures of the decomposition product at 400 °C. Again, one can discern large particles with sizes of several hundred nm and small, 20–50 nm sized, nanocrystals. A closer look reveals that the large particles do not represent w-ZnO single crystals but porous agglomerates of 20–40 nm sized nanocrystals, which, interestingly, show rather sharp edges at their boundaries. We conjecture that when annealing at 400 °C, water evaporated too quickly to allow the CPA growth of larger homogeneous crystals. Therefore, it would be interesting to perform decomposition experiments at various temperatures, different times, and also in a controlled atmosphere of humidities to explore the range of possible w-ZnO nanostructures from the decomposition of  $\text{Zn}_5(\text{OH})_{10}\cdot 2\text{H}_2\text{O}$ .

### 3. CONCLUSIONS

Hydrothermal conversion of  $\epsilon\text{-Zn}(\text{OH})_2$  at pressures between 1 and 2 GPa affords the zinc hydroxide hydrate  $\text{Zn}_5(\text{OH})_{10}\cdot 2\text{H}_2\text{O}$ , which represents a new LZH where, uniquely, the anion component corresponds to  $\text{OH}^-$ .  $\text{Zn}_5(\text{OH})_{10}\cdot 2\text{H}_2\text{O}$  features neutral zinc hydroxide layers, composed of octahedrally and tetrahedrally coordinated Zn ions with a 3:2 ratio, in which  $\text{H}_2\text{O}$  is intercalated. Interlayer  $\text{H}_2\text{O}$  molecules are strongly H-bonded to five surrounding OH groups and appear orientationally disordered.  $\text{Zn}_5(\text{OH})_{10}\cdot 2\text{H}_2\text{O}$  is metastable at standard ambient pressure and temperature. Its thermal decomposition occurs at very low temperatures, between 70 and 100 °C, and yields 5–15 nm sized hexagonal w-ZnO crystals that, depending on the conditions, may intergrow to two-dimensional, flake-like, crystals with sizes of several hundred nm.

### 4. METHODS

**4.1. Synthesis.**  $\epsilon\text{-Zn}(\text{OH})_2$  was prepared by adding 45 mL of a fresh 1 M NaOH solution at once to 15 mL of 0.33 M  $\text{ZnCl}_2$  solution at room temperature under vigorous stirring. Stirring was maintained for 1 h. The white precipitate was subsequently filtered, washed onto a vacuum glass filter with deionized (DI) water, and dried. The phase purity of  $\epsilon\text{-Zn}(\text{OH})_2$  was ascertained by powder X-ray diffraction and

thermogravimetric analysis prior to its use as a precursor in hydrothermal conversion experiments.

Experiments at 0.5–2 GPa were performed with a piston-cylinder-type pressure vessel with 45 mm internal diameter. Mixtures of about 150 mg (1.5 mmol) of  $\epsilon\text{-Zn}(\text{OH})_2$  and 1.5 g of DI water (80 mmol) were loaded into Teflon sample cells with 13 mm inner diameter and 15 mm height. Experiments targeting deuterated products employed heavy water  $\text{D}_2\text{O}$  (99.9 at % D, Sigma-Aldrich). The sample cell was inserted into a Teflon cell with 22 mm inner diameter and 23 mm height, which serves as an insulation layer between the thermocouple and electrical feedthroughs. The cells were thereafter inserted into a larger Teflon container of 39 mm internal diameter. The sample cell was sealed with a Teflon lid and tightly fitted into the piston-cylinder apparatus and, thereafter, the whole-cell assembly was transferred into a 1500 ton hydraulic press. The pressure in the cell was determined from the signal of an oil pressure gauge, which had previously been calibrated with an uncertainty of  $\pm 0.05$  GPa (at 2 GPa) in a separate experiment using the pressure dependence of the resistance of a manganin wire. Target temperatures were 100 and 200 °C and the temperature was measured by a calibrated chromel–alumel thermocouple with an estimated temperature uncertainty of  $\pm 1$  K. A typical compression rate of 0.3 GPa/h and a heating rate of 0.3 K/min were applied. After 2 h of annealing, experiments were quenched by switching off the external heater power. Subsequent decompression was performed at a rate 0.3 GPa/h.

Control experiments at/near ambient pressure were carried out using a stainless-steel autoclave.  $\epsilon\text{-Zn}(\text{OH})_2$ –water mixtures were loaded into Teflon liners with a dimension similar to that of the Teflon cell used in the piston-cylinder experiments. The sealed autoclave was placed inside an oven that was preheated to 100 or 200 °C, held at this temperature for 1 day, and then air-quenched to room temperature. Temperature was monitored with a thermocouple directly at the wall of the autoclave. Products recovered from the piston cylinder and autoclave runs were filtered, washed, and dried at room temperature.

## 4.2. Powder X-ray Diffraction (PXRD) Analysis.

Ambient-temperature powder X-ray diffraction (PXRD) patterns were collected on a Panalytical X'Pert Alpha diffractometer operated with Cu  $K\alpha_1$  radiation and in  $\theta$ – $2\theta$  diffraction geometry. Powder samples were mounted on a Si wafer zero-background holder and diffraction patterns were measured in a  $2\theta$  range 10–110° with a 0.013° step size. Powder patterns were indexed using DICVOL06<sup>34</sup> and McMaille programs.<sup>35</sup> Structure solution and Rietveld refinement were performed using FOX<sup>36</sup> and Fullprof Suite<sup>37</sup> software packages, respectively. During Rietveld refinement, the following parameters were refined: background, zero shift or sample displacement, scaling factor, unit cell parameters, peak profile and asymmetry, and both atom positions and isotropic temperature factors. A Thompson–Cox–Hastings pseudo-Voigt function was used for modeling the peak shape.

Multitemperature PXRD studies were performed using the XRK 900 chamber from Anton Paar, which was attached to a Panalytical X'Pert PRO instrument operating with Cu  $K\alpha$  radiation and in  $\theta$ – $2\theta$  diffraction geometry. The powdered sample was mounted on a gold sample holder. Measurements were performed in an air atmosphere up to 400 °C and data were collected in a  $2\theta$  range 18–38°. Each measurement had a 5 min equilibration time, a 45 min acquisition time, and a 5 °/min heating rate between the steps. Si powder was employed as an internal standard.

**4.3. Powder Neutron Diffraction Analysis.** Deuterated product was prepared at 2 GPa and 100 °C from a 1 M  $e$ -Zn(OH)<sub>2</sub>–D<sub>2</sub>O mixture and collected into a vial, which was filled with heavy water to the top. The vial was sealed to prevent isotope exchange from moist air. The sample was dried under air/moisture-free conditions under a flow of argon and subsequently transferred into a glovebox with an Ar atmosphere, where it was sealed in a quartz capillary (3 mm diameter) with vacuum grease and instant glue. The General Materials (GEM) diffractometer at the ISIS neutron and a muon source (STFC, United Kingdom) was used for collecting neutron powder diffraction data. The data were analyzed with program package GSAS-II.<sup>38</sup>

**4.4. Scanning Electron Microscopy (SEM) Investigations.** SEM imaging was performed using a JEOL JSM 7000F microscope equipped with a Schottky-type field emission gun. Powder samples were dispersed over a sticky carbon tape mounted on an aluminum stub and partially coated with a 10–15 nm gold layer to decrease the charging. Gold coating did not lead to any noticeable surface alterations.

**4.5. Transmission Electron Microscopy (TEM).** Transmission electron microscopy (TEM) morphological observations and in situ decomposition studies were performed on a JEOL 2100F instrument operating at 200 kV accelerating voltage. Morphological observations were made through conventional bright-field (BF) imaging. The in situ study comprised a combination of BF imaging and a time series of selected area electron beam diffraction (SAED) patterns. To reduce the electron beam damage and to slow down the decomposition rate during the data collection, a small condenser aperture (100  $\mu$ m) and spot size 3 were used. High-resolution TEM imaging was performed using the Themis Z TEM equipped with probe and image aberration correctors and a Gatan Oneview camera. The observation was made at 300 kV accelerating voltage using the Gatan 636 double-tilt cryogenic holder cooled with liquid nitrogen. Energy-dispersive X-ray (EDX) analysis was performed using

a JEOL 2100F microscope on powder samples deposited onto a copper microgrid coated with holey carbon. Electron energy loss spectroscopy (EELS) was performed with a GIF Tridiem spectrometer. All spectra were recorded with the 2 mm entrance aperture and with a dispersion of 0.2 eV per channel.

**4.6. Spectroscopy.** Attenuated total reflection Fourier transform infrared (ATR-FTIR) spectra were acquired on a Varian 610-IR FTIR spectrometer in the 400–4000  $\text{cm}^{-1}$  wavenumber range (32 scans, resolution 4  $\text{cm}^{-1}$ ) using a Specac Goldengate micro-ATR accessory equipped with KRS-5 lenses and a diamond ATR element. Spectra were normalized in a range from 0 to 1. Raman spectra were acquired on a LabRAM HR 800 Raman instrument equipped with an 800 mm focal length spectrograph and an air-cooled, back-thinned CCD detector (1024  $\times$  256 pixels with a size of 26  $\times$  26  $\mu\text{m}^2$ , spectral range 200–1050 nm). Samples were excited with an air-cooled double-frequency Nd:YAG laser (532 nm/50 mW). The edge and interference filters for measurements were <100  $\text{cm}^{-1}$ .

**4.7. Thermal Analysis.** Thermogravimetric (TG) experiments were performed using a TA Instruments Discovery system. Sample powders of about 4–7 mg were heated in a platinum crucible from room temperature up to 750 °C at a heating rate of 5 °C/min and a N<sub>2</sub> gas flow of 20 mL/min was applied. Differential scanning calorimetry (DSC) experiments were performed with a Netzsch DSC 214 Polyma instrument from –10 to 300 °C and otherwise using the same conditions as those for the TG experiments.

**4.8. Computational Investigations.** To explore possible hydrogen atom arrangements, the simulated annealing (SA) global optimization algorithm in Endeavour 1.7 software was employed.<sup>39</sup> Zn and O positions of the refined X-ray structure for Zn<sub>5</sub>(OH)<sub>10</sub>·2H<sub>2</sub>O were introduced as a base, to which H atoms were added. A simple repulsion potential for the charged ions was used during the optimization, while the positions of the Zn and O atoms were kept fixed. The minimal O–H and Zn–H distances were constrained to 0.9 and 2.45 Å, respectively. Several SA global optimization runs with 50–100 seeds were performed, which produced a range of structures with various H-atom arrangements. These structures were then subjected to density functional theory (DFT) optimization and their stability was assessed by comparing total energies. DFT total energy calculations were performed using Vienna Ab Initio Simulation Package (VASP)<sup>40,41</sup> in the framework of the projector augmented wave method (PAW)<sup>42</sup> within generalized gradient approximation (GGA), and employing the Perdew–Burke–Ernzerhof (PBE) parametrization of the exchange–correlation functional.<sup>43,44</sup> The cutoff energy for the plane wave basis set was 600 eV. Structural relaxations employed a 2  $\times$  2  $\times$  2  $\Gamma$ -centered k-point grid, and Brillouin zone integration was done with the tetrahedron method.<sup>45</sup> Forces on all atoms were converged to maximal 0.01 eV/Å.

## ■ ASSOCIATED CONTENT

### Supporting Information

The Supporting Information is available free of charge at <https://pubs.acs.org/doi/10.1021/acsomega.0c02075>.

TEM EEL spectroscopy and TEM EDX study of samples 2–100; thermochemical considerations for Zn<sub>5</sub>(OH)<sub>10</sub>·2H<sub>2</sub>O and DFT calculations of the pressure dependence of the enthalpy of formation reactions;



PXRD pattern of the product of the dry conversion of  $\epsilon$ -Zn(OH)<sub>2</sub> at high pressure; PXRD, ATR-FTIR, and TG analyses of the aged Zn<sub>5</sub>(OH)<sub>10</sub>·2H<sub>2</sub>O sample; ATR-FTIR and Raman spectra of the deuterated Zn<sub>5</sub>(OH)<sub>10</sub>·2H<sub>2</sub>O sample; parameters of the DFT optimized structure of Zn<sub>5</sub>(OH)<sub>10</sub>·2H<sub>2</sub>O; and TEM and HRTEM images of the decomposition product of Zn<sub>5</sub>(OH)<sub>10</sub>·2H<sub>2</sub>O annealed at 125 °C (PDF)

Frame-by-frame video of the Zn<sub>5</sub>(OH)<sub>10</sub>·2H<sub>2</sub>O transformation to w-ZnO as observed during an in situ TEM study (MP4)

Zn<sub>5</sub>(OH)<sub>10</sub>·2H<sub>2</sub>O (CIF)

## AUTHOR INFORMATION

### Corresponding Author

Ulrich Häussermann – Department of Materials and Environmental Chemistry, Stockholm University, SE-106 91 Stockholm, Sweden; [orcid.org/0000-0003-2001-4410](https://orcid.org/0000-0003-2001-4410); Email: [Ulrich.Haussermann@mmm.su.se](mailto:Ulrich.Haussermann@mmm.su.se)

### Authors

Alisa Gordeeva – Department of Materials and Environmental Chemistry, Stockholm University, SE-106 91 Stockholm, Sweden

Ying-Jui Hsu – Department of Physics, Umeå University, SE-901 87 Umeå, Sweden

Istvan Z. Jenei – Department of Materials and Environmental Chemistry, Stockholm University, SE-106 91 Stockholm, Sweden

Paulo H. B. Brant Carvalho – Department of Materials and Environmental Chemistry, Stockholm University, SE-106 91 Stockholm, Sweden

Sergei I. Simak – Theoretical Physics Division, Department of Physics, Chemistry and Biology (IFM) Linköping University, SE-581 83 Linköping, Sweden

Ove Andersson – Department of Physics, Umeå University, SE-901 87 Umeå, Sweden; [orcid.org/0000-0003-1748-9175](https://orcid.org/0000-0003-1748-9175)

Complete contact information is available at:

<https://pubs.acs.org/10.1021/acsomega.0c02075>

### Notes

The authors declare no competing financial interest.

## ACKNOWLEDGMENTS

This work was supported by the Swedish Research Council (VR) through grant 2016-04413 and Stiftelsen Olle Engkvist Byggmästare (SOEB). P.H.B.B.C. acknowledges support from the Swedish Foundation for Strategic Research (SSF) within the Swedish National Graduate School in neutron scattering (SwedNess). S.I.S. acknowledges support from the Swedish Government Strategic Research Area Grant in Materials Science on Functional Materials at Linköping University (Faculty Grant SFO-Mat-LiU No. 2009 00971) and the Swedish Research Council (VR) (Project No. 2019-05551). The computations were performed on resources provided by the Swedish National Infrastructure for Computing (SNIC) at High Performance Computing Center North (HPC2N). The experiment at the ISIS Neutron and Muon Source was enabled by beamtime allocation from the Science and Technology Facilities Council. We are grateful to Kristina Spektor (ESRF, Grenoble) for assistance in using Endeavor software and to

Ron Smith (ISIS neutron and muon source) for performing the neutron diffraction experiment on the GEM diffractometer.

## REFERENCES

- (1) Rives, V. *Layered Double Hydroxides: Present and Future*; Nova Science Publishers, Inc.: New York, 2001.
- (2) Arizaga, G. G. C.; Satyanarayana, K. G.; Wypych, F. Layered Hydroxide Salts: Synthesis, Properties and Potential Applications. *Solid State Ionics* **2007**, *178*, 1143–1162.
- (3) Mishra, G.; Dash, B.; Pandey, S. Layered Double Hydroxides: A Brief Review from Fundamentals to Application as Evolving Biomaterials. *Appl. Clay Sci.* **2018**, *153*, 172–186.
- (4) Shinagawa, T.; Watanabe, M.; Mori, T.; Tani, J.; Chigane, M.; Izaki, M. Oriented Transformation from Layered Zinc Hydroxides to Nanoporous ZnO: A Comparative Study of Different Anion Types. *Inorg. Chem.* **2018**, *57*, 13137–13149.
- (5) Evans, D. G.; Slade, R. C. T. Structural Aspects of Layered Double Hydroxides. In *Layered Double Hydroxides (Structure and Bonding)*; Springer-Verlag: Berlin, 2006; Vol. 119, pp 1–87.
- (6) Ståhlin, W.; Oswald, H. R. The Crystal Structure of Zinc Hydroxide Nitrate, Zn<sub>5</sub>(OH)<sub>8</sub>(NO<sub>3</sub>)<sub>2</sub>·2H<sub>2</sub>O. *Acta Crystallogr., Sect. B: Struct. Crystallogr. Cryst. Chem.* **1970**, *26*, 860–863.
- (7) Hawthorne, F. C.; Sokolova, E. Simonkolleite, Zn<sub>5</sub>(OH)<sub>8</sub>Cl<sub>2</sub>(H<sub>2</sub>O), a Decorated Interrupted Sheet Structure of the Form [Mφ<sub>2</sub>]<sub>4</sub>. *Can. Mineral.* **2002**, *40*, 939–946.
- (8) Miao, J.; Xue, M.; Itoh, H.; Feng, Q. Hydrothermal Synthesis of Layered Hydroxide Zinc Benzoate Compounds and Their Exfoliation Reactions. *J. Mater. Chem.* **2006**, *16*, 474–480.
- (9) Song, B.; Wang, Y.; Cui, X.; Kou, Z.; Si, L.; Tian, W.; Yi, C.; Wei, T.; Sun, Y. A Series of Unique Architecture Building of Layered Zinc Hydroxides: Self-Assembling Stepwise Growth of Layered Zinc Hydroxide Carbonate and Conversion into Three-Dimensional ZnO. *Cryst. Growth Des.* **2016**, *16*, 887–894.
- (10) Leung, A. H. M.; Pike, S. D.; Clancy, A. J.; Lee, W. J.; Orchard, K. L.; Shaffer, M. S. P.; Williams, C. K.; Yau, H. C. Layered Zinc Hydroxide Monolayers by Hydrolysis of Organozincs. *Chem. Sci.* **2018**, *9*, 2135–2146.
- (11) Inoue, S.; Fujihara, S. Liquid - Liquid Biphasic Synthesis of Layered Zinc Hydroxides Intercalated with Long-Chain Carboxylate Ions and Their Conversion into ZnO Nanostructures. *Inorg. Chem.* **2011**, *50*, 3605–3612.
- (12) Hosono, E.; Fujihara, S.; Honma, I.; Zhou, H. The Fabrication of an Upright-Standing Zinc Oxide Nanosheet for Use in Dye-Sensitized Solar Cells. *Adv. Mater.* **2005**, *17*, 2091–2094.
- (13) Moezzi, A.; McDonagh, A.; Dowd, A.; Cortie, M. Zinc Hydroxyacetate and Its Transformation to Nanocrystalline Zinc Oxide. *Inorg. Chem.* **2013**, *52*, 95–102.
- (14) Moezzi, A.; Cortie, M.; McDonagh, A. Transformation of Zinc Hydroxide Chloride Monohydrate to Crystalline Zinc Oxide. *Dalton Trans.* **2016**, *45*, 7385–7390.
- (15) Qin, N.; Xiang, Q.; Zhao, H.; Zhang, J.; Xu, J. Evolution of ZnO Microstructures from Hexagonal Disk to Prismoid, Prism and Pyramid and Their Crystal Facet-Dependent Gas Sensing Properties. *CrystEngComm* **2014**, *16*, 7062–7073.
- (16) Wang, M. S.; Zhou, Y. J.; Zhang, Y. P.; Hahn, S. H.; Kim, E. J. From Zn(OH)<sub>2</sub> to ZnO: A Study on the Mechanism of Phase Transformation. *CrystEngComm* **2011**, *13*, 6024–6026.
- (17) Jia, W.; Dang, S.; Liu, H.; Zhang, Z.; Yu, C.; Liu, X.; Xu, B. Evidence of the Formation Mechanism of ZnO in Aqueous Solution. *Mater. Lett.* **2012**, *82*, 99–101.
- (18) Nicholas, N. J.; Franks, G. V.; Ducker, W. A. The Mechanism for Hydrothermal Growth of Zinc Oxide. *CrystEngComm* **2012**, *14*, 1232–1240.
- (19) Wang, J.; Ma, P.; Xiang, L. Effects of NaOH on Formation of ZnO Nanorods from  $\epsilon$ -Zn(OH)<sub>2</sub>. *Mater. Lett.* **2015**, *141*, 118–121.
- (20) Lutz, H. D. Hydroxide Ions in Condensed Materials – Correlation of Spectroscopic and Structural Data. In *Structure and Bonding*; Springer-Verlag: Berlin, 1995; Vol. 82, pp 85–103.



- (21) Lutz, H. D.; Jung, C. Water Molecules and Hydroxide Ions in Condensed Materials; Correlation of Spectroscopic and Structural Data. *J. Mol. Struct.* **1997**, *404*, 63–66.
- (22) Klopogge, J. T.; Frost, R. L. Infrared and Raman Spectroscopic Studies of Layered Double Hydroxides (LDHs). In *Layered Double Hydroxides: Present And Future*; Nova Science Publishers Inc: New York, USA, 2001; pp 139–192.
- (23) Lutz, H. D.; Jung, C.; Mortel, R.; Jacobs, H.; Stahl, R. Hydrogen Bonding in Solid Hydroxides with Strongly Polarising Metal Ions,  $\beta$ -Be(OH)<sub>2</sub> and  $\epsilon$ -Zn(OH)<sub>2</sub>. *Spectrochim. Acta, Part A* **1998**, *54*, 893–901.
- (24) Stahl, R.; Jung, C.; Lutz, H. D.; Kockelmann, W.; Jacobs, H. Kristallstrukturen Und Wasserstoffbrückenbindungen Bei  $\beta$ -Be(OH)<sub>2</sub> Und  $\epsilon$ -Zn(OH)<sub>2</sub>. *Z. Anorg. Allg. Chem.* **1998**, *624*, 1130–1136.
- (25) Srivastava, O. K.; Secco, E. A. Studies on Metal Hydroxy Compounds. II. Infrared Spectra of Zinc Derivatives  $\epsilon$ -Zn(OH)<sub>2</sub>,  $\beta$ -ZnOHCl, ZnOHF, Zn<sub>5</sub>(OH)<sub>8</sub>Cl<sub>2</sub>, and Zn<sub>5</sub>(OH)<sub>8</sub>Cl<sub>2</sub>·H<sub>2</sub>O. *Can. J. Chem.* **1967**, *45*, 585–588.
- (26) Shaporev, A. S.; Ivanov, V. K.; Baranchikov, A. E.; Polezhaeva, O. S.; Tret'yakov, Y. D. ZnO Formation under Hydrothermal Conditions from Zinc Hydroxide Compounds with Various Chemical Histories. *Russ. J. Inorg. Chem.* **2007**, *52*, 1811–1816.
- (27) Srivastava, O. K.; Secco, E. A. Studies on Metal Hydroxy Compounds. I. Thermal Analyses of Zinc Derivatives  $\epsilon$ -Zn(OH)<sub>2</sub>, Zn<sub>5</sub>(OH)<sub>8</sub>Cl<sub>2</sub>·H<sub>2</sub>O,  $\beta$ -ZnOHCl, and ZnOHF. *Can. J. Chem.* **1967**, *45*, 579–583.
- (28) Kogure, T. Dehydration Sequence of Gibbsite by Electron-Beam Irradiation in a TEM. *J. Am. Ceram. Soc.* **1999**, *82*, 716–720.
- (29) Löffler, L.; Mader, W. Transformation Mechanism of the Dehydration of Diaspore. *J. Am. Ceram. Soc.* **2003**, *86*, 534–540.
- (30) Miehe, G.; Lauterbach, S.; Kleebe, H.; Gurlo, A. Indium Hydroxide to Oxide Decomposition Observed in One Nanocrystal during in Situ Transmission Electron Microscopy Studies. *J. Solid State Chem.* **2013**, *198*, 364–370.
- (31) De Yoreo, J. J.; Gilbert, P. U. P. A.; Sommerdijk, N. A. J. M.; Penn, R. L.; Whitlam, S.; Joester, D.; Zhang, H.; Rimer, J. D.; Navrotsky, A.; Banfield, J. F.; Wallace, A. F.; Michel, F. M.; Meldrum, F. C.; Cölfen, H.; Dove, P. M. Crystallization by Particle Attachment in Synthetic, Biogenic, and Geologic Environments. *Science* **2015**, *349*, No. aaa6760.
- (32) Audebrand, N.; Auffredic, J.-P.; Louer, D. X-Ray Diffraction Study of the Early Stages of the Growth of Nanoscale Zinc Oxide Crystallites Obtained from Thermal Decomposition of Four Precursors. General Concepts on Precursor-Dependent Microstructural Properties. *Chem. Mater.* **1998**, *10*, 2450–2461.
- (33) Hosono, E.; Tokunaga, T.; Ueno, S.; Oaki, Y.; Imai, H.; Zhou, H.; Fujihara, S. Crystal-Growth Process of Single-Crystal-like Mesoporous ZnO through a Competitive Reaction in Solution. *Cryst. Growth Des.* **2012**, *12*, 2923–2931.
- (34) Boulton, A.; Louer, D. Program for the Automatic Indexing of Powder Diffraction Patterns by the Successive Dichotomy Method. *J. Appl. Crystallogr.* **2004**, *37*, 724–731.
- (35) Le Bail, A. Monte Carlo Indexing with McMaille. *Powder Diffr.* **2004**, *19*, 249–254.
- (36) Favre-nicolin, V.; Cern, R. FOX, “Free Objects for Crystallography”: A Modular Approach to Ab Initio Structure Determination from Powder Diffraction. *J. Appl. Crystallogr.* **2002**, *35*, 734–743.
- (37) Rodríguez-Carvajal, J. *Fullprof: A Program for Rietveld Refinement and Pattern Matching Analysis*, Abstract of the Satellite Meeting on Powder Diffraction of the XV Congress of the IUCr, Toulouse, France, 1990.
- (38) Toby, B. H.; Von Dreele, R. B. GSAS-II: The Genesis of a Modern Open-Source All Purpose Crystallography Software Package. *J. Appl. Crystallogr.* **2013**, *46*, 544–549.
- (39) Putz, H.; Schoen, J. C.; Jansen, M. Combined Method for “Ab Initio” Structure Solution from Powder Diffraction Data. *J. Appl. Crystallogr.* **1999**, *32*, 864–870.
- (40) Kresse, G.; Hafner, J. Ab Initio Molecular Dynamics for Liquid Metals. *Phys. Rev. B* **1993**, *47*, 558–561.
- (41) Kresse, G.; Furthmu, J. Efficient Iterative Schemes for Ab Initio Total-Energy Calculations Using a Plane-Wave Basis Set. *Phys. Rev. B* **1996**, *54*, No. 11169.
- (42) Blochl, P. E. Projector Augmented-Wave Method. *Phys. Rev. B* **1994**, *50*, 953–979.
- (43) Perdew, J. P.; Burke, K.; Ernzerhof, M. Generalized Gradient Approximation Made Simple. *Phys. Rev. Lett.* **1996**, *77*, 3865–3868.
- (44) Perdew, J. P.; Burke, K.; Ernzerhof, M. Generalized Gradient Approximation Made Simple. *Phys. Rev. Lett.* **1997**, *78*, No. 1396.
- (45) Blöchl, P. E.; Jepsen, O.; Andersen, O. K. Improved Tetrahedron Method for Brillouin-Zone Integrations. *Phys. Rev. B* **1994**, *49*, 16223–16233.